

RESEARCH ARTICLE

Three-Dimensional Muscle Architecture and Comprehensive Dynamic Properties of Rabbit Gastrocnemius, Plantaris and Soleus: Input for Simulation Studies

Tobias Siebert^{1*}, Kay Leichsenring¹, Christian Rode², Carolin Wick², Norman Stutzig¹, Harald Schubert³, Reinhard Blickhan², Markus Böhl⁴

1 Department of Sport and Motion Science, University of Stuttgart, Stuttgart, Germany, **2** Institute of Motion Science, Friedrich-Schiller-University Jena, Jena, Germany, **3** Institut für Versuchstierkunde und Tierschutz, Universitätsklinikum Jena, Jena, Germany, **4** Institute of Solid Mechanics, Technical University at Braunschweig, Braunschweig, Germany

* tobias.siebert@inspo.uni-stuttgart.de



OPEN ACCESS

Citation: Siebert T, Leichsenring K, Rode C, Wick C, Stutzig N, Schubert H, et al. (2015) Three-Dimensional Muscle Architecture and Comprehensive Dynamic Properties of Rabbit Gastrocnemius, Plantaris and Soleus: Input for Simulation Studies. PLoS ONE 10(6): e0130985. doi:10.1371/journal.pone.0130985

Editor: Renzhi Han, Ohio State University Medical Center, UNITED STATES

Received: March 4, 2015

Accepted: May 26, 2015

Published: June 26, 2015

Copyright: © 2015 Siebert et al. This is an open access article distributed under the terms of the [Creative Commons Attribution License](http://creativecommons.org/licenses/by/4.0/), which permits unrestricted use, distribution, and reproduction in any medium, provided the original author and source are credited.

Data Availability Statement: All relevant data are within the paper and its Supporting Information files.

Funding: This work was supported by the Deutsche Forschungsgemeinschaft (<http://www.dfg.de/>) under Grants BO 3091/4 to MB, and SI 841/3 to TS. The funders had no role in study design, data collection and analysis, decision to publish, or preparation of the manuscript.

Competing Interests: The authors have declared that no competing interests exist.

Abstract

The vastly increasing number of neuro-muscular simulation studies (with increasing numbers of muscles used per simulation) is in sharp contrast to a narrow database of necessary muscle parameters. Simulation results depend heavily on rough parameter estimates often obtained by scaling of one muscle parameter set. However, *in vivo* muscles differ in their individual properties and architecture. Here we provide a comprehensive dataset of dynamic ($n = 6$ per muscle) and geometric (three-dimensional architecture, $n = 3$ per muscle) muscle properties of the rabbit calf muscles gastrocnemius, plantaris, and soleus. For completeness we provide the dynamic muscle properties for further important shank muscles (flexor digitorum longus, extensor digitorum longus, and tibialis anterior; $n = 1$ per muscle). Maximum shortening velocity (normalized to optimal fiber length) of the gastrocnemius is about twice that of soleus, while plantaris showed an intermediate value. The force-velocity relation is similar for gastrocnemius and plantaris but is much more bent for the soleus. Although the muscles vary greatly in their three-dimensional architecture their mean pennation angle and normalized force-length relationships are almost similar. Forces of the muscles were enhanced in the isometric phase following stretching and were depressed following shortening compared to the corresponding isometric forces. While the enhancement was independent of the ramp velocity, the depression was inversely related to the ramp velocity. The lowest effect strength for soleus supports the idea that these effects adapt to muscle function. The careful acquisition of typical dynamical parameters (e.g. force-length and force-velocity relations, force elongation relations of passive components), enhancement and depression effects, and 3D muscle architecture of calf muscles provides valuable comprehensive datasets for e.g. simulations with neuro-muscular models, development of more realistic muscle models, or simulation of muscle packages.

Introduction

About 600 skeletal muscles enable complex movements like locomotion or laughing in humans. Musculoskeletal models with an increasing number of muscles have been used to investigate human and animal movements [1–4]. Although many phenomenological Hill-type [5–8] and biophysical [9, 10] muscle models have been developed to represent the dynamics of isolated muscles, the phenomenological modeling approach dominates in musculoskeletal modeling for simplicity and low computational cost. Because individual muscle parameters are lacking, a common approach in such studies is to scale one set of muscle parameters, e.g. by maximum isometric force and fiber length, to fit all muscles [2–4]. However, muscles differ in their individual muscle properties not only by scale, and these differences impact simulation results [11].

The active contractile properties of muscle fibers can be characterized by the hyperbolic force–velocity relation [5] and the force–length relation [12]. It has generally been found that slow twitch fibers exhibit a more bent force–velocity relation and lower maximum shortening velocity than fast ones [13]. Moreover, it is known that muscles exhibit a complex architecture consisting of fascicles with different lengths and pennation angles [14–16]. The specific architecture influences the shape of the muscle’s force–length relation [17]. Thus, simple scaling of these relations introduces errors of unknown magnitude. A broader database of lumped muscle model parameters for specific muscles would improve the situation; in parallel, development of more realistic three-dimensional (3D) muscle models requires individual muscle architecture as input [18–20].

Passive muscle properties vary considerably between muscles too [21]. For instance, passive forces of frog gastrocnemius arise already on the ascending limb of the force–length relation and reach about 30% maximum isometric force (F_{im}) at optimal muscle length [22]. In contrast, passive forces of the frog semitendinosus muscle arise on the descending limb of the force–length relation [23]. Depending on muscle function tendons exhibit different mechanical properties [24], e.g. the tendon of the human wrist mover *M. extensor carpi radialis longus* used for positioning tasks is very stiff (1.8% strain at F_{im} , [25]) compared with the more compliant human gastrocnemius tendon exploited for elastic recoil (5% strain at F_{im} , [26]).

In Hill-type muscle models, the active contractile properties of the fibers are represented by a contractile component (CC). Its length is usually taken to be the mean optimal fiber length, and sometimes the mean pennation angle is considered [6]. Passive tissues in parallel to the fibers like connective tissue and titin (though titin may be considered to be a semi-active element, [27]) can be represented by a parallel elastic component (PEC). Tendon and aponeurosis thought to act in series with the fibers [22] are represented by a serial elastic component (SEC). In the structurally more convincing arrangement of these three components [28] the SEC is in series to both the CC and the PEC (Fig 1). Typical constitutive functions describing the components are depicted in Fig 1.

Since more than 60 years it is known that muscle force further depends on contraction history [30]. For example, force is enhanced in the isometric phase following active stretching (force enhancement, FE) and depressed following active shortening (force depression, FD) compared with the corresponding isometric muscle force. Force enhancement effects can be much larger ($2 F_{im}$ at lengths with no filament overlap, [31]) than force depression effects (0.05 – $0.2 F_{im}$, [30, 32]). Currently, the causes of these history effects remain a matter of scientific debate [8, 33–35]. Discussed mechanisms are e.g. the contribution of half-sarcomere chain dynamics [34, 36, 37] or non-cross-bridge contributions to muscle tension [27, 31, 38]. Muscle specific differences in contraction history are rarely examined, particularly as experimental protocols and conditions differ, which hampers comparison.

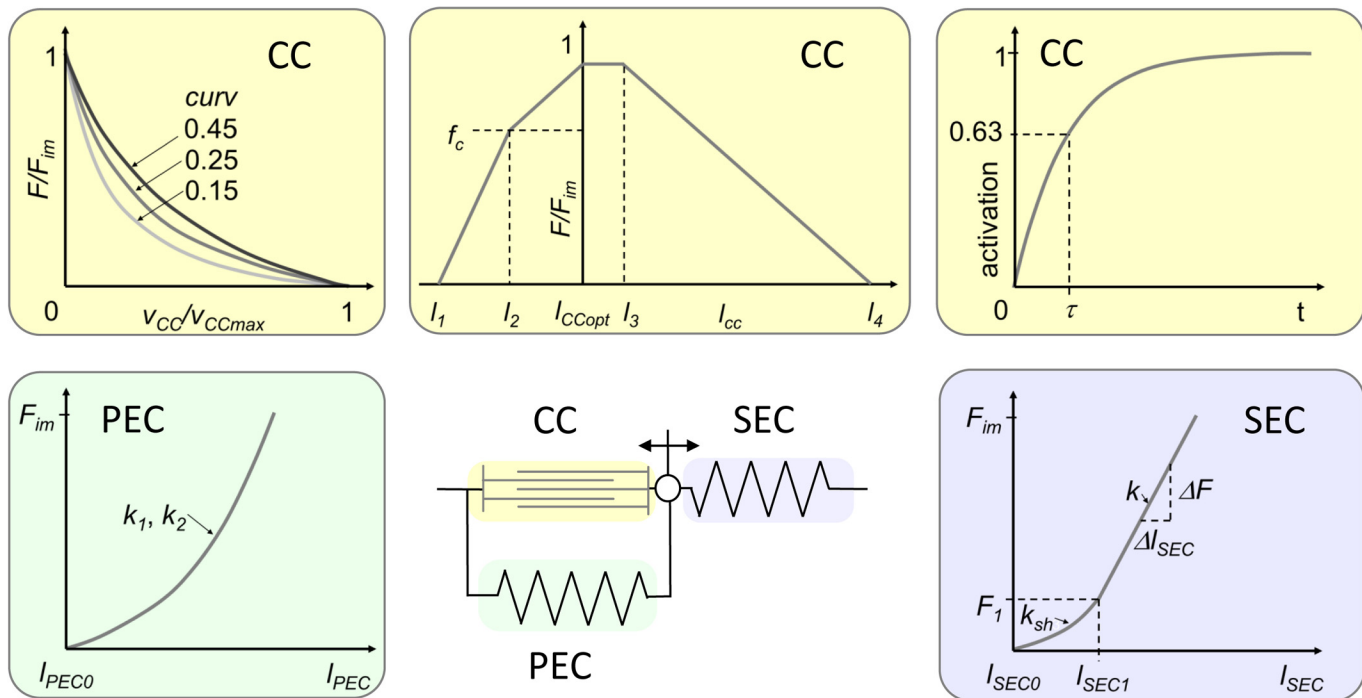


Fig 1. Hill-type muscle model and associated muscle properties. The muscle model [28, 29] for which the parameters are determined in this study consists of a contractile component (CC), a serial elastic component (SEC) and a parallel elastic component (PEC). Muscle components and associated muscle properties (force-velocity relation, force-length relation, activation-time relation, force-elongation relation of SEC and PEC) are marked with the same background color. Corresponding model parameters are explained in section 2.3.

doi:10.1371/journal.pone.0130985.g001

The calf musculature is frequently used as a research object in muscle experiments and simulations (gastrocnemius (GAS), soleus (SOL) and/or plantaris (PLA); e.g. [21, 39–41]). These distal muscles enable comparably easy surgical access, and their long distal tendons simplify fixation to force measurement equipment in animal models. Some of these muscles were observed in recent *in vivo* studies with respect to their 3D behavior [42, 43]. Understanding e.g. 3D muscle deformations and related force effects in muscle packages by neuromuscular simulations requires consistent specific muscle properties and muscle architectures. Gained insights into fundamental 3D muscle functions may then be generalized which makes the collection of comprehensive data sets important from a clinical perspective. To our knowledge, such comprehensive consistent muscle properties are not available for the calf musculature.

The aim of this study is to provide comprehensive data sets of specific muscle properties (force-length relation, force-velocity relation, force-strain relations of SEC and PEC, activation time constant) and the 3D architecture of the superficial rabbit calf muscles for future research. To achieve this, we determine muscle properties of GAS, PLA, and SOL in *in situ* experiments ($n = 6$ per muscle) and measure the 3D architecture by manual digitization ([16]; $n = 3$ per muscle). Because there is no generally accepted model of history effects, we provide standardized data for force enhancement and force depression ($n = 3$ per muscle) which can be used to adapt parameters of custom models describing these effects. Striving for completeness with respect to the shank musculature (Fig 2), we provide the muscle properties for further shank muscles (flexor digitorum longus (FDL), extensor digitorum longus (EDL) and tibialis anterior (TA), $n = 1$).

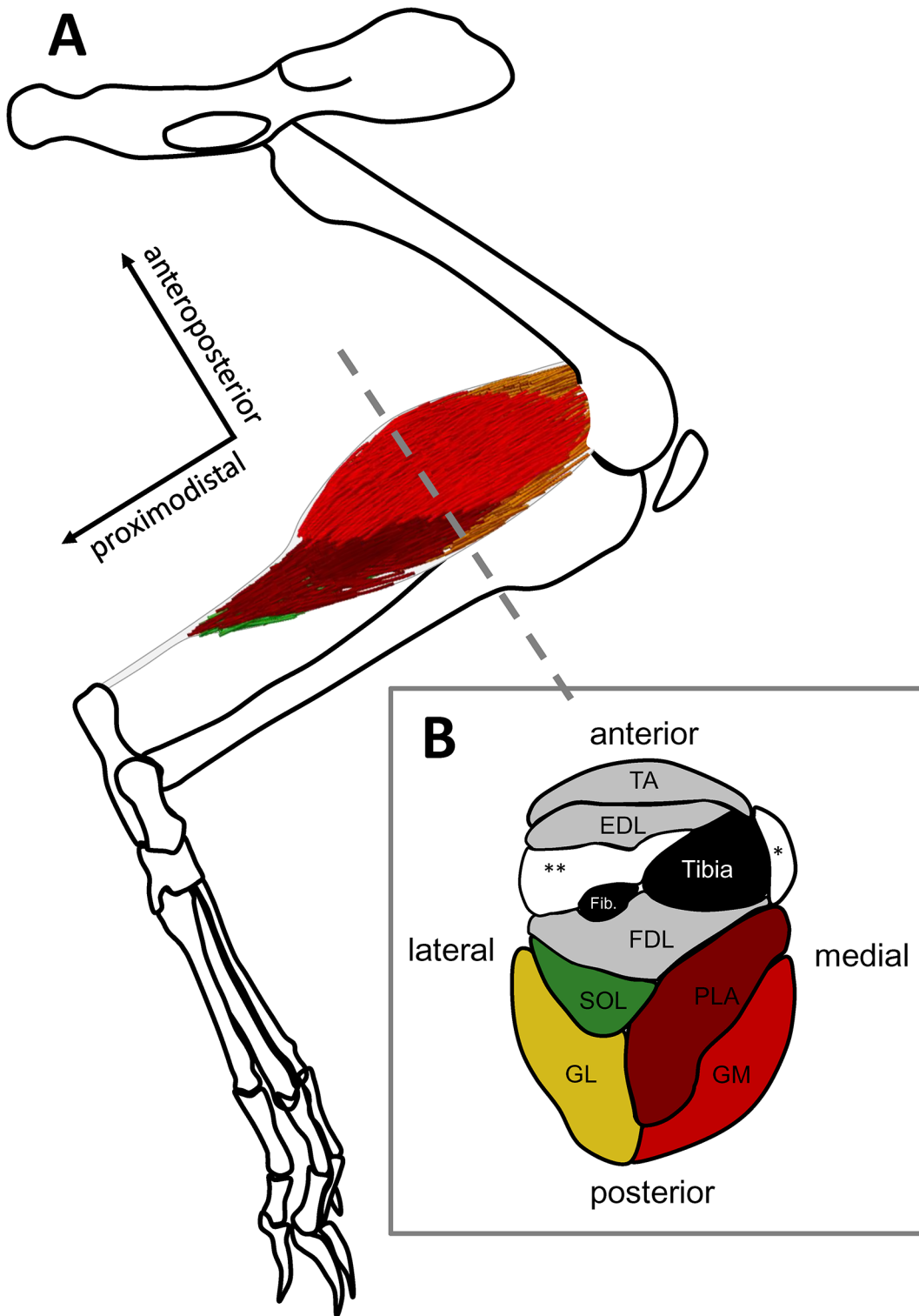


Fig 2. Schematic of the rabbit calf muscles. (A) Medial view of the left pelvic limb and the calf muscles whose dynamic muscle properties and architecture have been determined (GAS, PLA, SOL). The grey dashed line marks the transversal cross-section of the limb shown in (B). For the grey muscles (FDL, EDL, and TA), only dynamic muscle properties were determined (see [Supporting Information, S1 Text](#)). White muscles (***peroneae* muscles, * *M. extensor hallucis longus*) were not examined. The axes are shown for orientation.

doi:10.1371/journal.pone.0130985.g002

Methods

2.1 Experimental setup

Experiments on female New Zealand white rabbits (*Oryctolagus cuniculus*, $n = 21$, age: about 16 weeks) with an average weight of 3.37 ± 0.51 kg (mean \pm SD, Table 1) were carried out in strict accordance with the recommendations of the German animal welfare law (Tierschutzgesetz, BGBl. I 1972, 1277, section 8). The protocol of this study was approved by the competent authority for animal welfare in Thuringia, Germany (Landesamt für Verbraucherschutz (Abteilung Gesundheitlicher und technischer Verbraucherschutz); Permit Number: 02-022/11 and 02-027/14). All experiments were performed under anesthesia with natrium pentobarbital (Nembutal, 80 mg/kg body weight) and Bupivacain (1 ml, 0.5%, epidural), and all efforts were made to minimize suffering. Experimental setup, anesthesia and preparation of rabbit SOL have been described earlier [43]. Procedures were similar for all muscles analyzed in this study (Table 1). In short, the specific muscle was freed from its surrounding tissues and the rabbit was fixed by clamping hip, knee and ankle with three pairs of bone pins. The distal tendon was attached horizontally to a muscle lever system (Aurora scientific 310B-LR). The sciatic nerve was stimulated (Aurora Scientific 701C) with 100 μ s square wave pulses at 100–140 Hz (supra-maximal tetanic muscle stimulation). Body temperature was maintained at 39°C using a heating pad. The muscle was sprinkled with heated (39°C) physiological saline solution during the entire experiment.

2.2 Experiments for determination of muscle properties

First, the muscle-tendon complex length (L_{MTC_0}) was measured *in situ* with a micrometer at an ankle and knee joint angle of 90° (Table 1). To determine the specific muscle properties (force-length relation, force-velocity relation, force-strain relation of the SEC and PEC, and activation time constant), isometric, isotonic and isokinetic contractions were performed. We identified the force-velocity relation by a series of about 10 isotonic contractions against forces in the range of $0.1 F_{im}$ to $0.9 F_{im}$. Similar to [44], the force-strain relation of the SEC was obtained from the length tension data of a quick (exceeding maximum contraction velocity v_{CCmax}) isokinetic contraction accounting for fiber shortening. The active force-length relation of the CC and the force-strain relation of the PEC were determined from a series of 15–20 isometric contractions (with length increments of 1–2 mm) considering the interaction of the passive elastic structures [28]. The activation parameter τ , describing calcium concentration and thus muscle activation, was determined from an isometric contraction at optimal muscle length using a Hill-type model [29]. For details of these parameter determinations, see [29, 45].

Table 1. Specifications of observed muscles.

Muscle	GAS	PLA	SOL	FDL	EDL	TA
Dynamic muscle properties (n)	6	6	6	1	1	1
animal mass [kg]	3.02 ± 0.39	3.27 ± 0.22	3.89 ± 0.47	2.76	3.52	3.38
muscle mass [g]	16.04 ± 1.32	6.31 ± 0.74	3.26 ± 0.32	4.78	4.77	3.52
L_{MTC_0} [mm]	118.2 ± 6.2	112.0 ± 6.6	102.9 ± 2.0	104.2	103.4	91.9
3D muscle architecture (n)	3	3	3	N/A	N/A	N/A
animal mass [kg]	$3.28 \pm 0.17^*$	$3.28 \pm 0.17^*$	$3.28 \pm 0.17^*$	N/A	N/A	N/A

Muscle and animal mass as well as the muscle-tendon complex length L_{MTC_0} measured at ankle and knee joint angles of 90° (cf. Fig 1). n : number of muscles.

*Architecture of GAS, PLA, and SOL was determined from the left legs of three rabbits.

doi:10.1371/journal.pone.0130985.t001

History effects were identified for GAS, PLA, and SOL ($n = 3$ per muscle) using isokinetic ramps [32] with three different shortening / lengthening velocities (0.35, 0.7, and $1.4 l_{fm}/s$, where l_{fm} is the mean fascicle length determined by manual digitization; see section 2.4), and a ramp length of $0.3 l_{fm}$. The isokinetic ramp started after an isometric pre-contraction (200 to 400 ms) which was sufficient to reach maximum isometric force. After the end of the ramp, stimulation continued (SOL: 1300 ms; other muscles: 500 ms) to allow sufficient force recovery during the subsequent isometric phase. Longer continued stimulation was used for SOL because this slow twitch fibered muscle [46] is more fatigue resistant than the other muscles. Shortening and lengthening ramps for determination of force depression and force enhancement started at optimum muscle length plus $0.15 l_{fm}$ and minus $0.15 l_{fm}$, respectively. Force depression and force enhancement were identified as the difference in force between the force at the end of the ramp experiment and the force at the end of an isometric reference contraction of same duration at the same target length. For FDL, EDL, and TA no muscle architecture and thus no mean fascicle length (l_{fm}) was determined. Thus, for these muscles isokinetic ramps had velocities of 5, 10 and 20 mm/s starting at optimum muscle length plus 2 mm (force depression) and minus 2 mm (force enhancement) with a ramp length of 4 mm.

2.3 Hill-type muscle model

Parameters were determined for a typical Hill-type muscle model [29] consisting of a PEC in parallel to the CC, and a SEC connected to both of them. Using this model, the active force generated by the contractile component F_{cc} is the difference between the single forces in the SEC and the PEC and can be described by a typical product approach [6]:

$$F_{CC} = F_{SEC} - F_{PEC} = A \cdot F_{im} \cdot f_l(l_{CC}) \cdot f_v(v_{CC}). \tag{1}$$

In Eq (1), A is the muscle activation and f_l as well as f_v are factors that describe the force-length and force-velocity relations normalized to F_{im} , respectively.

The CC force-length relationship was described with a piecewise linear equation

$$f_l(l_{CC}) = \begin{cases} \frac{f_c}{l_2 - l_1} \cdot (l_{CC} - l_1), & l_1 \leq l_{CC} \leq l_2 \\ f_c + \frac{f_c - 1}{l_2} \cdot (l_{CC} - l_2), & l_2 < l_{CC} \leq l_{CCopt} \\ 1, & l_{CCopt} < l_{CC} \leq l_3 \\ 1 + \frac{-1}{l_4 - l_3} \cdot (l_{CC} - l_3), & l_3 < l_{CC} \leq l_4 \end{cases} \tag{2}$$

where f_c is the force at which the ascending limb changes slope, l_{CC} is the CC length, l_{CCopt} the optimal CC length and l_1, l_2, l_3, l_4 are specific lengths that are crucial for the sarcomere force-length relationship (Fig 1).

The force-velocity relationship

$$f_v(v_{CC}) = \frac{v_{CCmax} - v_{CC}}{v_{CCmax} + v_{CC}/curv} \quad v_{CC} < 0, \tag{3}$$

follows the Hill hyperbola [5] for concentric contractions, with v_{CCmax} being the maximal CC shortening velocity, and $curv = a/F_{im}$ (damping increases with decreasing $curv$, see Fig 1; a describes the force asymptote [5]) is an inverse measure of the relation's curvature.

The latency between the supramaximal stimulation and the muscle activation was modelled as a first order linear differential equation [47]

$$\frac{dA}{dt} = \frac{1 - A}{\tau} \tag{4}$$

where the activation parameter τ lumps the time constants of calcium influx from the sarcoplasmic reticulum into the sarcoplasm, and $A(t = 0) = 0$.

The SEC force-elongation relationship $F_{SEC}(\Delta l_{SEC})$ was taken from [6]

$$F_{SEC}(\Delta l_{SEC}) = \frac{F_1}{e^{k_{sh}} - 1} \cdot \left(e^{\frac{k_{sh} \cdot \Delta l_{SEC}}{\Delta l_{SEC1}}} - 1 \right), \quad 0 < \Delta l_{SEC} < \Delta l_{SEC1} \tag{5}$$

$$F_{SEC}(\Delta l_{SEC}) = F_1 + k \cdot (\Delta l_{SEC} - \Delta l_{SEC1}), \quad \Delta l_{SEC1} \leq \Delta l_{SEC}$$

where Δl_{SEC1} and F_1 are the elongation and the force at which the force-elongation relation changes from exponential to linear. k was calculated from Δl_{SEC1} , F_1 , the dimensionless shape parameter k_{sh} and the constraint that stiffness at $\Delta l_{SEC} = \Delta l_{SEC1}$ is the same for each equation.

A PEC force-elongation relation

$$F_{PEC}(\Delta l_{PEC}) = k_1 \cdot (e^{k_2 \cdot \Delta l_{PEC}} - 1), \quad \text{if } \Delta l_{PEC} > 0 \tag{6}$$

depending on k_1 and k_2 was taken from [48].

2.4 Determination of muscle architecture

Muscle architecture of GAS, PLA, and SOL was determined from the left legs of three rabbits (R1 to R3, $m = 3.28 \pm 0.17$ kg) by manual digitization [16, 43]. After the rabbit was killed with an overdose of pentobarbital, the leg was amputated above the knee. The skin was removed and the preparation fixed in Bouin solution (an aqueous solution of picric acid, acetic acid and formaldehyde minimizing tissue shrinkage [49, 50]) for 48 h [14] at knee and ankle angles of about 79° and 93°, respectively. Subsequently, the bone-muscle preparation was cast in wax to provide additional mechanical stability during the digitizing process. For the digitization of the whole muscle architecture of each muscle, small fascicle bundles were successively dissected with a micro forceps. Their original position was then recorded using a manual 3D digitizer (MicroScribe MLX) with a sampling frequency of 5 Hz and an accuracy of 0.07 mm. This process was repeated until all fascicles of the individual muscle were recorded. Each fascicle was described by 20 points. During the dissection and the digitizing, the palm of the hand holding the digitizer-handpiece was placed on the preparation-table to minimize movement of the digitizer tip (< 0.1 mm). Fascicle length and pennation angle were calculated as described in [16]. In addition to recording the fascicle bundle positions, the insertions and origins of the muscles were recorded for each animal (S1, S5, and S9 Datasets).

2.5 Statistics

Prior to analysis, muscle parameters were normalized using pertinent units. Parameters were tested for normal distribution using the Kolmogorov-Smirnov-Test with Lilliefors correction. All data were normally distributed. The Levené test was used to check variance homogeneity. To test whether muscle properties differ between the muscles (GAS, PLA, SOL) an analysis of variance (ANOVA) was calculated. In case that the ANOVA demonstrated significant main effects, post hoc analyses were performed using the Tukey HSD test if variances were homogenous. Otherwise the Tamhane test was used. The significance level was set at $P < 0.05$. All

analyses were performed using SPSS 22 (IBM Corp, Armonk, NY, USA). The effect sizes f were calculated as

$$f = \frac{\sigma_m}{\sigma}, \quad (7)$$

where σ_m is the standard deviation of the population means, and σ the within-population standard deviation [51]. The effect sizes were classified as low ($f = 0.1$), medium ($f = 0.25$) and large ($f > 0.40$) [51].

Results

3.1 Muscle properties

Active and passive muscle properties vary considerably between GAS, PLA, and SOL. We found significant differences for the parameters l_{CCopt} , v_{CCmax} , $curv$, $\Delta l_{SEC1}/l_{SEC0}$, k , l_{SEC0} , and l_{PECO} (Table 2). All experimental force–velocity relationships feature the typical hyperbolic shape (Fig 3, second row) observed by [5]. Maximum shortening velocity of GAS ($13.5 \pm 1.7 l_{CCopt}/s$) is about twice the value of SOL ($6.4 \pm 1.0 l_{CCopt}/s$). Maximum shortening velocity of PLA ($10.1 \pm 3.3 l_{CCopt}/s$) is in between these values. The $curv$ values of the force-velocity relation are similar for GAS and PLA (0.47 ± 0.09 and 0.41 ± 0.16 , respectively) but about three times the value for SOL (0.15 ± 0.05). The calf muscles exhibited a characteristic force–length dependency (Fig 3, upper row) which is attributable to the muscle fiber force–length relationship [12]. Maximum isometric forces produced at optimum muscle lengths by GAS, PLA, and SOL are 161.3 ± 18.2 N, 86.4 ± 21.3 N, and 24.1 ± 5.8 N, respectively. Considering a muscle tissue density of 1.056 g/cm^3 [52], as well as a mean muscle mass (Table 1) and mean optimal fiber length (Table 2), the cross-sectional area (CSA) can be calculated (GAS: 8.63 cm^2 , PLA: 4.57 cm^2 , SOL: 1.44 cm^2). This leads to similar mean muscle stresses of 18.9, 18.8, and 17.0 N/cm^2 for GAS, PLA, and SOL, respectively. Optimum fiber lengths of SOL ($22.1 \pm 4.5 \text{ mm}$) are longer than those of PLA ($13.2 \pm 1.3 \text{ mm}$) enabling a much larger working range of SOL. Series and parallel elastic components possess typical [6] nonlinear force–strain characteristics (Fig 3). The standard deviations of the determined muscle properties are small, with the exception of the force–strain relation of the parallel elastic component (Fig 3, bottom row) which is about three times the standard deviation observed for the SEC.

Forces of GAS, PLA, and SOL were enhanced following stretching and were depressed following shortening compared with the corresponding isometric forces (Table 2, Fig 4). For all muscles, force depression was inversely related to the ramp velocity (Table 2). This effect was pronounced for the SOL. In contrast, force enhancement was independent of ramp velocity. The magnitude of force enhancement increased from GAS ($\approx 8\% F_{im}$), to SOL ($\approx 11\% F_{im}$) up to PLA ($\approx 17\% F_{im}$). At the slowest ramp velocity ($0.35 l_{fm}/s$), force depression of GAS and PLA ($\approx 17.5\% F_{im}$) was about two fold that of SOL ($9.7\% F_{im}$).

We report additionally obtained muscle properties of further shank muscles (FDL, EDL, TA; $n = 1$) for completeness in the Supporting Information (S1 Text).

3.2 Architecture

General architectural properties of GAS, PLA, and SOL are listed in Table 3. Spatial coordinates of the fascicles of rabbit R1 are presented in Fig 5. Three dimensional fascicle data including origin and insertion of the GAS, PLA, and SOL of the three animals (R1, R2, R3) are provided in txt-format in the Supporting Information (S1–S12 Datasets). SOL (Fig 5, green fascicles) exhibits simple unipennate muscle architecture while GAS (*medialis*: light red fascicles; *lateralis*: yellow fascicles) and PLA (dark red fascicles) show more complex bipennate muscle

Table 2. Muscle parameters of GAS, PLA, and SOL.

	Muscle	GAS	PLA	SOL	p	f-value
	Parameter	mean ± S.D.	mean ± S.D.	mean ± S.D.		
f_l	l_1 / l_{CCopt}	0.44 ± 0.11	0.53 ± 0.06	0.50 ± 0.05	ns	-
	l_2 / l_{CCopt}	0.82 ± 0.07	0.88 ± 0.04	0.82 ± 0.03	ns	-
	l_3 / l_{CCopt}	1.14 ± 0.03	1.19 ± 0.07	1.14 ± 0.04	ns	-
	l_4 / l_{CCopt}	2.21 ± 0.21	2.05 ± 0.21	1.95 ± 0.42	ns	-
	$f_c [F_{im}]$	0.85 ± 0.08	0.85 ± 0.07	0.85 ± 0.05	ns	-
	$F_{im} / CSA [N/cm^2]$	18.9 ± 3.3	18.8 ± 3.1	17.0 ± 4.3	ns	-
	$l_{CCopt} [mm]$	17.7 ± 1.1	13.2 ± 1.3	22.1 ± 4.5	0.01 (*, †)	1.30
f_v	$v_{CCmax} [l_{CCopt}/s]$	13.5 ± 1.7	10.1 ± 3.3	6.4 ± 1	0.01 (†, #)	1.29
	$curv$	0.47 ± 0.09	0.41 ± 0.16	0.15 ± 0.05	0.01 (†, #)	1.25
A	$\tau [s]$	0.06 ± 0.03	0.06 ± 0.03	0.04 ± 0.01	ns	-
SEC	F_1 / F_{im}	0.31 ± 0.06	0.31 ± 0.09	0.43 ± 0.14	ns	-
	$\Delta l_{SEC1} / l_{SEC0}$	0.049 ± 0.009	0.036 ± 0.006	0.026 ± 0.004	0.00 (*, #)	1.42
	k_{sh}	2.2 ± 0.3	2.6 ± 0.5	2.7 ± 0.7	ns	-
	$k [N/mm]$	30.3 ± 1.4	21.9 ± 4.9	14.1 ± 2.7	0.00 (*, †, #)	2.01
	$l_{SEC0} [mm]$	105.3 ± 5.2	102 ± 5.6	86.9 ± 2.7	0.00 (†, #)	1.79
PEC	$k_1 [N]$	0.048 ± 0.057	0.114 ± 0.171	0.034 ± 0.031	ns	-
	$k_2 [mm^{-1}]$	0.50 ± 0.18	0.47 ± 0.17	0.35 ± 0.12	ns	-
	$l_{PECO} [mm]$	12.9 ± 2.9	9.8 ± 1.9	16.0 ± 1.8	0.00 (*, †, #)	1.41
FD	FD _{0.35} [% F_{im}]	17.3 ± 0.9	17.8 ± 4.8	9.7 ± 1.2		
	FD _{0.7} [% F_{im}]	16.6 ± 0.7	15.4 ± 4.0	8.0 ± 0.9		
	FD _{1.4} [% F_{im}]	16.0 ± 0.7	14.6 ± 3.9	5.8 ± 1.5		
FE	FE _{0.35} [% F_{im}]	7.7 ± 1.6	17.1 ± 9.6	11.3 ± 1.5		
	FE _{0.7} [% F_{im}]	7.7 ± 1.4	17.0 ± 9.8	11.3 ± 1.7		
	FE _{1.4} [% F_{im}]	7.7 ± 1.6	17.0 ± 8.7	11.2 ± 1.3		

Mean and standard deviation of muscle specific properties; f_l : force-length relation, f_v : force-velocity relation, A: muscle activation, SEC: series elastic component, PEC: parallel elastic component. Force depression (FD) and force enhancement (FE) were determined for three different velocities (0.35, 0.7, and 1.4 mean fascicle lengths per second). Significant differences are marked as follows

* $p < 0.05$ between GAS and PLA

† $p < 0.05$ between PLA and SOL

$p < 0.05$ between SOL and GAS.

ns means not significant. The effect sizes were classified as low ($f = 0.1$), medium ($f = 0.25$) and large ($f > 0.40$) [51]. No statistics was performed for FD and FE due to small sample size ($n = 3$).

doi:10.1371/journal.pone.0130985.t002

architectures. For each animal, the mean pennation angles of all three muscles (GAS, PLA, and SOL) were almost similar (Table 3). Differences appear to be about 1–2°, only. In between the different animals, variations were slightly larger. Mean pennation angles in R1 are about 5° larger than in R3. These variations in pennation angles have only small ($< 0.02 F_{im}$) impact on the calculation of muscle force. Mean fascicle lengths (l_{fm}) are larger for the heavier animals (R2 and R3). For each specific animal, GAS and SOL exhibit about the same mean fascicle lengths but in general PLA is about 30% shorter.

Discussion

Experiments performed within this study provide comprehensive data sets for the rabbit calf muscles GAS, PLA, and SOL consisting of manually digitized 3D muscle architectures and specific muscle properties including the quantification of history effects.

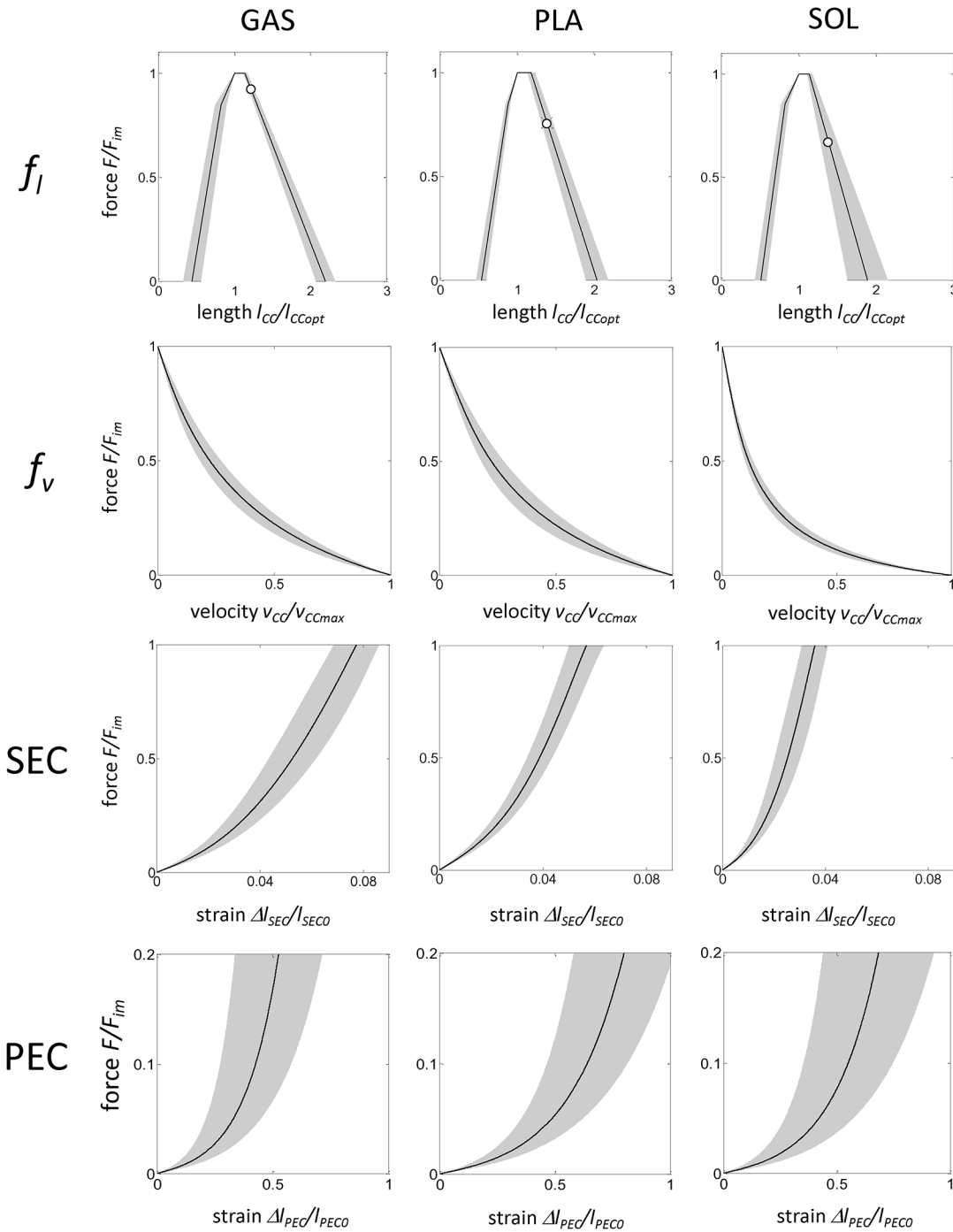


Fig 3. Muscle properties of GAS, PLA, and SOL. The black curves indicate mean values, whereas the grey areas depict the standard deviations. First row: force–length (f_l) relation. F_{im} is the maximum isometric muscle force, l_{CC} and l_{CCopt} are the length and the optimal length of the contractile component, respectively. To avoid muscle damage, the muscles were lengthened until passive forces reached about $0.2 F_{im}$ (marked with a white circle). Second row: force–velocity (f_v) relation. v_{CCmax} is the maximal shortening velocity of the contractile component. Third row: Force–strain relation of the series elastic component (SEC). Δl_{SEC} and l_{SEC0} are the length change and the slack length of the series elastic component, respectively. Last row: Force–strain relation of the parallel elastic component (PEC). Δl_{PEC} and l_{PEC0} are the length change and the slack length of the parallel elastic component, respectively.

doi:10.1371/journal.pone.0130985.g003

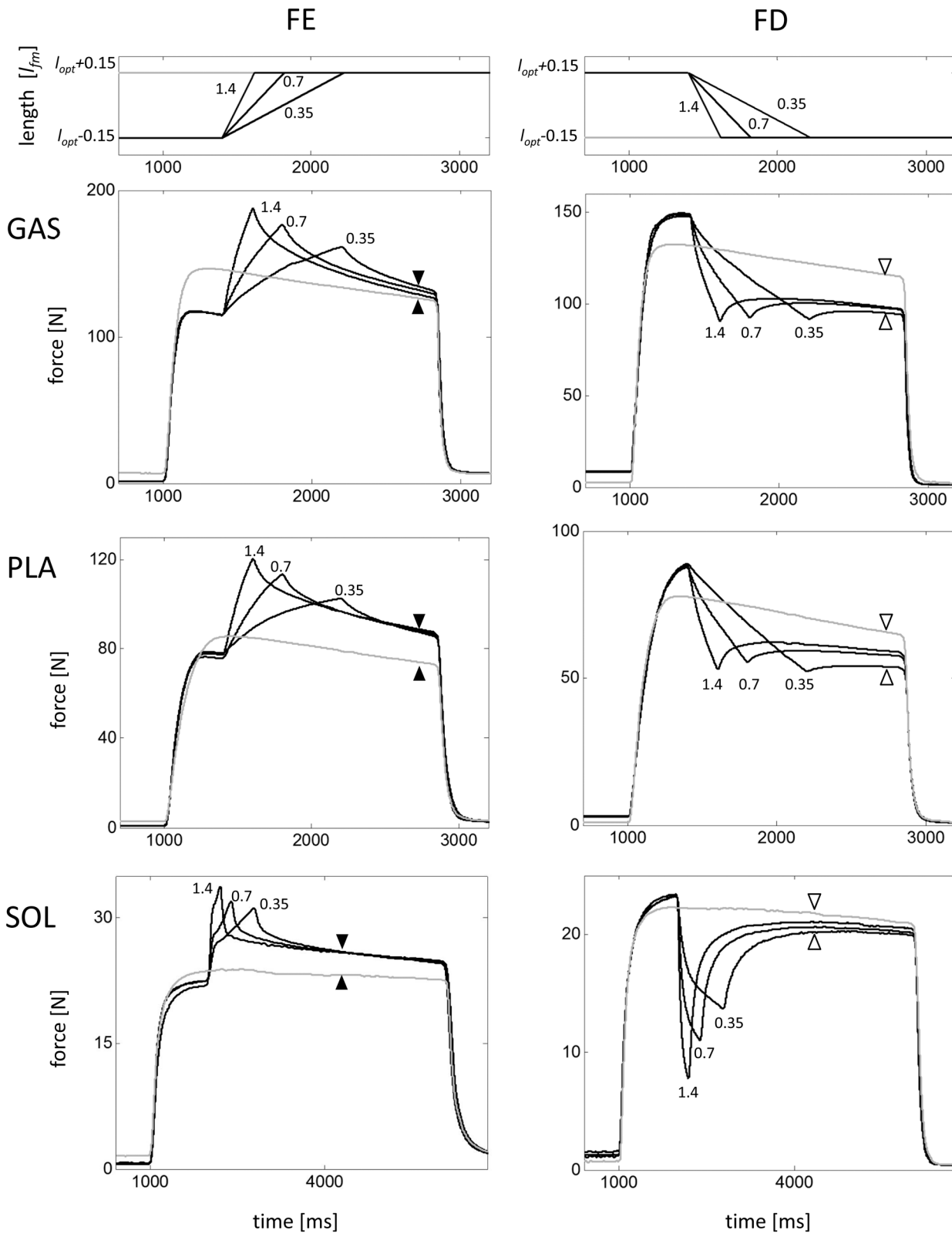


Fig 4. Force enhancement (FE) and force depression (FD) experiments. Typical experiments are shown for one GAS ($m = 14.8$ g), SOL ($m = 3.3$ g), and PLA ($m = 7.5$ g), respectively. Exemplary isokinetic ramps are depicted for GAS in the top row; numbers without units indicate velocity in mean fascicle lengths per second. FE (difference between black triangles) and FD (difference between white triangles) are the force difference between ramp experiment

(black) and isometric reference contraction (grey) determined 500ms (GAS, PLA) and 1300ms (SOL) after the end of the ramp, shown exemplarily for the slowest (0.35 l_{fm}/s) ramp.

doi:10.1371/journal.pone.0130985.g004

4.1 Comparison with literature: muscle properties

Mean muscle tensions of GAS, PLA, and SOL determined in this study are comparable to values between 14 and 20 N/cm² observed for other small mammal muscles, e.g. rat SOL [53, 54], rabbit SOL [43], rat GAS medialis [45], kangaroo rat PLA [55], or guinea pig SOL [53].

SOL maximum shortening velocity and *curv* value of the force-velocity relation (Table 2) are similar to values reported for slow twitch muscles (v_{CCmax} : 3–7 l_{CCopt}/s , *curv*: 0.1–0.2, [13, 29, 56]). Higher shortening velocities and *curv* values of GAS and PLA agree with values reported for fast twitch muscles (v_{CCmax} : 9–20 l_{CCopt}/s , *curv*: 0.3–0.5, [13, 56, 57]). These results are in agreement with fiber type compositions of rabbit GAS (> 75% fast twitch fibers), PLA (> 90% fast twitch fibers), and SOL (> 99% slow twitch fibers; [46, 58]).

The active force-length relation was described by the theoretical sarcomere force-length relationship [12]. As demonstrated in recent studies [28, 59] this relation enabled the accurate prediction of experimental rabbit and cat muscle forces. Winters [59] reproduced the active force-length relations of rabbit TA, EDL, and extensor digitorum II based on myofibril lengths using a scaled sarcomere model. In contrast, we fitted the experimental force-length data using a piecewise linear equation. However, the results are consistent for the most part. Starting from optimum muscle length, the rabbit muscles were able to shorten by 50% in both studies. For lengthening muscle, force production is limited to 1.6 l_{CCopt} in the scaled sarcomere model, but reaches about 2 l_{CCopt} for GAS, PLA, and SOL (Fig 3). Differences might be due to more complex muscle architectures, especially of GAS and PLA (Fig 5, see Sect. 4.2), influencing the width of the force-length relation [60]. Also, to avoid muscle damage induced by high passive forces, muscles in our study were lengthened only up to passive forces of about 0.2 F_{im} (Fig 3, upper row, marked by a white circle). Thus, the slope of the descending limb of the force length relation was determined using limited experimental data and should be considered with caution. The change in slope at the ascending limb of the force-length relation is fixed at 0.7 F_{im} in the scaled sarcomere model, but appears at higher forces ($f_c = 0.85 F_{im}$) in our measurements. However, the change in slope of experimental TA force-length relations appears at

Table 3. Muscle architecture of GAS, PLA, and SOL.

animal	muscle	mean pennation angle [°]	mean fascicle length l_{fm} [mm]	ankle joint angle [°]	knee joint angle [°]
R1 (m = 3.04 kg)	GAS	16.6 ± 7.3	14.1 ± 2.2	94	75
	PLA	16.1 ± 6.2	10.8 ± 2.1	94	75
	SOL	15.8 ± 5.4	14.0 ± 2.2	94	75
R2 (m = 3.10 kg)	GAS	14.5 ± 6.4	17.2 ± 3.3	93	91
	PLA	14.8 ± 6.3	11.1 ± 2.5	93	91
	SOL	12.0 ± 3.6	17.0 ± 2.2	93	91
R3 (m = 3.10 kg)	GAS	12.3 ± 5.2	19.3 ± 3.2	92	70
	PLA	11.1 ± 4.8	14.4 ± 3.1	92	70
	SOL	11.3 ± 3.5	20.4 ± 3.1	92	70

Mean pennation angle and fascicle length determined from the left legs of three rabbits (R1, R2, R3) by manual digitization. 1838, 1773, and 1523 fascicles have been digitized for R1, R2, and R3, respectively. Their lengths and pennation angles are normally distributed. The muscle architecture is exemplarily shown for R1 in Fig 5. Note that the complete 3D data are provided in the Supporting Information (S1–S12 Datasets).

doi:10.1371/journal.pone.0130985.t003

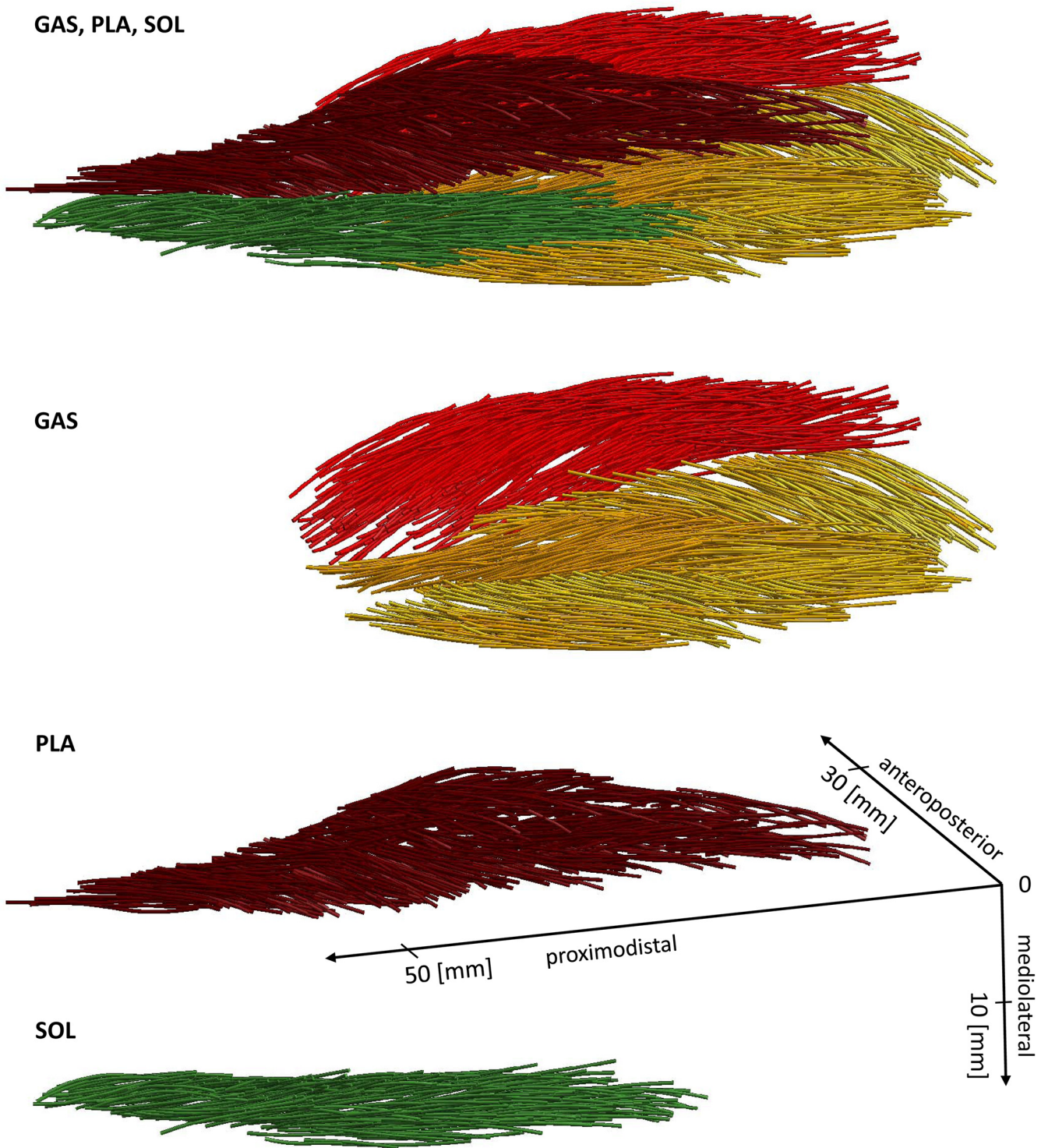


Fig 5. Muscle architectures of GAS, PLA, and SOL of R1 left pelvic limb. Muscle fascicles of GAS medialis and lateralis are shown in light red and yellow, respectively. The proximodistal axis corresponds to the mean force axis of the calf muscles, running from mean muscle origin at the humerus to the insertion at the calcaneus. The corresponding 3D data of the muscle fascicles are provided in the Supporting Information (S2–S4 Datasets).

doi:10.1371/journal.pone.0130985.g005

higher forces in the study of [59] (their Fig 3A) which is in agreement with our observations on TA (S1 Table).

Series elastic structures exhibit a typical [6] nonlinear force-strain relationship (Fig 3, third row). The mean maximum strain at F_{im} was 5.5% and 3.6% L_{SECO} for PLA and SOL (Fig 3), respectively, which is expected for tendinous tissue [61, 62]. The SEC of the GAS was more compliant (7.7% strain at F_{im}). This may be due to a higher proportion of aponeuroses in the muscle tendon complex which may be more compliant than tendons [63].

The standard deviations of the determined muscle properties are small, with the exception of the force-strain relation of the parallel elastic component (Fig 3, lower row). This has also been reported for other muscles [43, 64, 65] and may be related to variations in connective tissues (fascia, epimysium, perimysium, endomysium) or titin-isoforms (e.g. [66]).

The behavior of the rabbit muscles observed in this study is mostly consistent with history effects observed in other muscles. As found in our study, force enhancement is independent of stretch velocity [67], and force depression decreases with increasing ramp velocity [30]. The influence of these history effects on the determination of the muscle properties is discussed in the Supporting Information (S2 Text).

Using the same experimental setup and conditions we found muscle specific differences in the amount and in the ratio of force enhancement and force depression (Table 3, S1 Table). These muscle specific properties might be explained by synthesis of different titin isoforms in different rabbit muscles as reported by [66]. Interestingly, these differences in titin isoforms are not related to the fiber type. Interaction of titin with the actin myofilament is assumed to be responsible for the history dependence of muscle contractions [8, 27]. However, experimental and modeling evidence is necessary to demonstrate the conceivable relation between muscle specific titin isoforms and muscle specific history dependence of muscle contraction.

The mechanism and function of contraction history effects are a matter of scientific debate [8, 33–35]. Force enhancement enables the muscle to withstand high forces during eccentric contractions. Rode [27] suggested that force depression is an unwanted by-product of desired force enhancement, and does not occur in stretch-shortening cycles associated with bouncing gaits. The biarticular PLA has comparably short muscle fibers (Table 2) and long tendons, and is appropriate to work as a spring during hopping [58, 68]. Indeed, PLA exhibits comparably high force enhancement (Table 2) which enables generating high forces during eccentric contractions. However, the primary function of muscles working as motors during locomotion, e.g. the monoarticular SOL, is to produce positive work [41, 69, 70]. For these muscles force depression seems to be counterproductive because it reduces positive work. Indeed, SOL exhibited much lower force depression than GAS and PLA (Table 2). These findings support the idea that history effects represent an adaptation to the specific muscle function [27].

4.2 Muscle architecture

Studies providing 3D architectural data of muscle packages consisting of several synergistic muscles are rare. Using diffusion tensor imaging 3D muscle architecture of e.g. the human calf [71], human thigh [72], human forearm [73] and mouse hindlimb muscles [74] have been examined. The architecture of the human back [75] and cavy forelimb muscles [14] was determined by manual digitization. However, to the author's best knowledge, there is no consistent 3D data set of the complete rabbit calf muscle architecture.

Measurements comparable to our experiments were performed on rabbit SOL [43]. The authors examined ten SOL muscles using manual digitization and reported a mean fascicle length of 16.6 ± 2.6 mm which is similar to our value obtained from three muscles (17.1 ± 2.6 mm). A slightly lower mean pennation angle ($9.9 \pm 2.8^\circ$ vs. $13.0 \pm 2.0^\circ$) might be due to smaller

ankle joint angles reported in their study. In agreement with our results, Hiepe [76] reported mean fascicle lengths of 16.2 ± 9.1 mm for rabbit GAS *medialis* using DTI. The higher standard deviation in their study might be due to limitations of the diffusion tensor imaging method, e.g. generated fiber tracts may cross muscle borders due to equally oriented adjacent structures, resulting in artificial fascicle traces that are too long [16, 74].

There are few studies dealing with architectural measurements of the PLA [77–80]. None of them utilizes the rabbit as animal model or provides 3D architectural data what makes a direct comparison of fiber lengths and pennation angle impossible. Savelberg [78] mentioned that the non-parallel arrangement of the aponeuroses inside the rat's PLA features different pennation angles and various fiber lengths. This is in agreement with our observations of the complex bipennate rabbit PLA muscle architecture.

Models of muscle packages are required to understand transverse interaction of muscles with each other [81–83] and with the skeleton, internal muscle forces, and the influence of muscle architecture on contraction dynamics and muscle deformation. In addition to deviating muscle architectures, observed significant differences in normalized dynamical muscle parameters suggest that it is important to use specific muscle parameters in neuromuscular models aiming at understanding fundamental 3D muscle functions. The revelation of such fundamental 3D muscle functions may be relevant from a clinical perspective when assessing the effects of muscle malfunction e.g. on the stabilization of joints during movement. Moreover, 3D muscle models may contribute to a deeper understanding of widespread diseases as chronic low back pain which are accompanied by several changes in the muscle structure as atrophy [84], steatosis [85] or altered fiber type distribution [86].

Supporting Information

[S2–S12](#) Datasets (except S5 and S9) can be processed using GID software (CIMNE, Barcelona, Spain).

S1 Dataset. Rabbit R1: Origins and insertion of GAS, PLA, and SOL in txt-format.
(TXT)

S2 Dataset. Rabbit R1: GAS 3D muscle architecture in txt-format.
(TXT)

S3 Dataset. Rabbit R1: PLA 3D muscle architecture in txt-format.
(TXT)

S4 Dataset. Rabbit R1: SOL 3D muscle architecture in txt-format.
(TXT)

S5 Dataset. Rabbit R2: Origins and insertion of GAS, PLA, and SOL in txt-format.
(TXT)

S6 Dataset. Rabbit R2: GAS 3D muscle architecture in txt-format.
(TXT)

S7 Dataset. Rabbit R2: PLA 3D muscle architecture in txt-format.
(TXT)

S8 Dataset. Rabbit R2: SOL 3D muscle architecture in txt-format.
(TXT)

S9 Dataset. Rabbit R3: Origins and insertion of GAS, PLA, and SOL in txt-format.
(TXT)

S10 Dataset. Rabbit R3: GAS 3D muscle architecture in txt-format.
(TXT)

S11 Dataset. Rabbit R3: PLA 3D muscle architecture in txt-format.
(TXT)

S12 Dataset. Rabbit R3: SOL 3D muscle architecture in txt-format.
(TXT)

S1 Table. Muscle parameters of FDL, EDL and TA.
(DOCX)

S1 Text. Muscle properties of flexor digitorum longus (FDL), extensor digitorum longus (EDL), and tibialis anterior (TA).
(DOCX)

S2 Text. Influence of contraction history on the determination of muscle properties.
(DOCX)

Acknowledgments

This work was supported by the Deutsche Forschungsgemeinschaft (DFG) under Grants BO 3091/4-1,2 and SI 841/3-1,2.

Author Contributions

Conceived and designed the experiments: TS MB RB HS. Performed the experiments: KL CW TS HS. Analyzed the data: KL CW CR NS. Wrote the paper: TS CR NS.

References

1. Holzbaur KR, Murray WM, Delp SL. A model of the upper extremity for simulating musculoskeletal surgery and analyzing neuromuscular control. *Ann Biomed Eng.* 2005; 33(6):829–40. Epub 2005/08/05. PMID: [16078622](#).
2. Neptune RR, Sasaki K, Kautz SA. The effect of walking speed on muscle function and mechanical energetics. *Gait Posture.* 2008; 28(1):135–43. Epub 2007/12/26. doi: S0966-6362(07)00269-X [pii] doi: [10.1016/j.gaitpost.2007.11.004](#) PMID: [18158246](#).
3. Bobbert MF, Richard Casius LJ, Kistemaker DA. Humans make near-optimal adjustments of control to initial body configuration in vertical squat jumping. *Neuroscience.* 2013; 237:232–42. Epub 2013/02/07. doi: [10.1016/j.neuroscience.2013.01.055](#) S0306-4522(13)00099-7 [pii]. PMID: [23384608](#).
4. Rupp TK, Ehlers W, Karajan N, Gunther M, Schmitt S. A forward dynamics simulation of human lumbar spine flexion predicting the load sharing of intervertebral discs, ligaments, and muscles. *Biomech Model Mechanobiol.* 2015. Epub 2015/02/06. doi: [10.1007/s10237-015-0656-2](#) PMID: [25653134](#).
5. Hill AV. The Heat of Shortening and the Dynamic Constants of Muscle. *Proceedings of the Royal Society of London Series B, Biological Sciences.* 1938; 126(843):136–95.
6. Winters JM. Hill-based muscle models: A systems engineering perspective. In: Winters JM, Woo SLY, editors. *Multiple Muscle Systems.* New York: Springer Verlag; 1990. p. 69–93.
7. McGowan CP, Neptune RR, Herzog W. A phenomenological model and validation of shortening-induced force depression during muscle contractions. *J Biomech.* 2010; 43(3):449–54. Epub 2009/11/03. doi: S0021-9290(09)00567-3 [pii] doi: [10.1016/j.jbiomech.2009.09.047](#) PMID: [19879585](#).
8. Siebert T, Rode C. Computational modeling of muscle biomechanics. In: Jin Z, editor. *Computational Modelling of Biomechanics and Biotribology in the Musculoskeletal System.* Biomaterials and Tissues. 1st ed. Amsterdam: Woodhead Publishing / Elsevier; 2014. p. 173–243.
9. Huxley AF. Muscle structure and theories of contraction. *Prog Biophys Biophys Chem.* 1957; 7:255–318. Epub 1957/01/01. PMID: [13485191](#).
10. Zahalak GI. A comparison of the mechanical behavior of the cat soleus muscle with a distribution-moment model. *J Biomech Eng.* 1986; 108(2):131–40. Epub 1986/05/01. PMID: [3724100](#).

11. Neptune RR, McGowan CP, Fiandt JM. The influence of muscle physiology and advanced technology on sports performance. *Annu Rev Biomed Eng.* 2009; 11:81–107. Epub 2009/04/30. doi: [10.1146/annurev-bioeng-061008-124941](https://doi.org/10.1146/annurev-bioeng-061008-124941) PMID: [19400707](https://pubmed.ncbi.nlm.nih.gov/19400707/).
12. Gordon AM, Huxley AF, Julian FJ. The variation in isometric tension with sarcomere length in vertebrate muscle fibres. *J Physiol.* 1966; 184(1):170–92. PMID: [5921536](https://pubmed.ncbi.nlm.nih.gov/5921536/)
13. Ranatunga KW, Thomas PE. Correlation between shortening velocity, force-velocity relation and histochemical fibre-type composition in rat muscles. *J Muscle Res Cell Motil.* 1990; 11(3):240–50. PMID: [2401724](https://pubmed.ncbi.nlm.nih.gov/2401724/)
14. Gorb S, Fischer MS. 3D-analysis of the arrangement and length distribution of fascicles in the triceps muscle of the Galea musteloides (Rodentia, Cavimorpha). *Zoomorphology.* 2000; 120:91–7.
15. Blemker SS, Asakawa DS, Gold GE, Delp SL. Image-based musculoskeletal modeling: applications, advances, and future opportunities. *J Magn Reson Imaging.* 2007; 25(2):441–51. PMID: [17260405](https://pubmed.ncbi.nlm.nih.gov/17260405/).
16. Schenk P, Siebert T, Hiepe P, Gullmar D, Reichenbach JR, Wick C, et al. Determination of three-dimensional muscle architectures: validation of the DTI-based fiber tractography method by manual digitization. *J Anat.* 2013; 223(1):61–8. Epub 2013/05/18. doi: [10.1111/joa.12062](https://doi.org/10.1111/joa.12062) PMID: [23678961](https://pubmed.ncbi.nlm.nih.gov/23678961/).
17. Woittiez RD, Huijting PA, Rozendal RH. Influence of muscle architecture on the length-force diagram of mammalian muscle. *Pflugers Arch.* 1983; 399(4):275–9. PMID: [6664830](https://pubmed.ncbi.nlm.nih.gov/6664830/).
18. Röhrle O, Davidson JB, Pullan AJ. A physiologically based, multi-scale model of skeletal muscle structure and function. *Front Physiol.* 2012; 3:358. Epub 2012/09/21. doi: [10.3389/fphys.2012.00358](https://doi.org/10.3389/fphys.2012.00358) PMID: [22993509](https://pubmed.ncbi.nlm.nih.gov/22993509/); PubMed Central PMCID: PMC3440711.
19. Böl M, Weikert R, Weichert C. A coupled electromechanical model for the excitation-dependent contraction of skeletal muscle. *J Mech Behav Biomed Mater.* 2011; 4(7):1299–310. Epub 2011/07/26. doi: S1751-6161(11)00100-7 [pii] doi: [10.1016/j.jmbbm.2011.04.017](https://doi.org/10.1016/j.jmbbm.2011.04.017) PMID: [21783139](https://pubmed.ncbi.nlm.nih.gov/21783139/).
20. Böl M, Sturmat M, Weichert C, Kober C. A new approach for the validation of skeletal muscle modelling using MRI data. *Comput Mech.* 2011; 47:591–601.
21. Gareis H, Solomonow M, Baratta R, Best R, D'Ambrosia R. The isometric length-force models of nine different skeletal muscles. *J Biomech.* 1992; 25(8):903–16. PMID: [1639834](https://pubmed.ncbi.nlm.nih.gov/1639834/).
22. Epstein M, Herzog W. *Theoretical Models of Skeletal Muscle.* Chichester: John Wiley & Sons; 1998.
23. Wagner H, Siebert T, Ellerby DJ, Marsh RL, Blickhan R. ISOFIT: a model-based method to measure muscle-tendon properties simultaneously. *Biomech Model Mechanobiol.* 2005; 4(1):10–9. PMID: [15895262](https://pubmed.ncbi.nlm.nih.gov/15895262/).
24. Shadwick RE. Elastic energy storage in tendons: mechanical differences related to function and age. *J Appl Physiol* (1985). 1990; 68(3):1033–40. Epub 1990/03/01. PMID: [2341331](https://pubmed.ncbi.nlm.nih.gov/2341331/).
25. Loren GJ, Lieber RL. Tendon biomechanical properties enhance human wrist muscle specialization. *J Biomech.* 1995; 28(7):791–9. Epub 1995/07/01. doi: 0021-9290(94)00137-S [pii]. PMID: [7657677](https://pubmed.ncbi.nlm.nih.gov/7657677/).
26. Arampatzis A, Stafilidis S, DeMonte G, Karamanidis K, Morey-Klapsing G, Bruggemann GP. Strain and elongation of the human gastrocnemius tendon and aponeurosis during maximal plantarflexion effort. *J Biomech.* 2005; 38(4):833–41. PMID: [15713305](https://pubmed.ncbi.nlm.nih.gov/15713305/).
27. Rode C, Siebert T, Blickhan R. Titin-induced force enhancement and force depression: a 'sticky-spring' mechanism in muscle contractions? *J Theor Biol.* 2009; 259(2):350–60. Epub 2009/03/25. doi: S0022-5193(09)00114-3 [pii] doi: [10.1016/j.jtbi.2009.03.015](https://doi.org/10.1016/j.jtbi.2009.03.015) PMID: [19306884](https://pubmed.ncbi.nlm.nih.gov/19306884/).
28. Rode C, Siebert T, Herzog W, Blickhan R. The effects of parallel and series elastic components on the active cat soleus force-length relationship. *Journal of Mechanics in Medicine and Biology.* 2009; 9(1):105–22.
29. Siebert T, Rode C, Herzog W, Till O, Blickhan R. Nonlinearities make a difference: comparison of two common Hill-type models with real muscle. *Biol Cybern.* 2008; 98(2):133–43. PMID: [18049823](https://pubmed.ncbi.nlm.nih.gov/18049823/).
30. Abbott BC, Aubert XM. The force exerted by active striated muscle during and after change of length. *J Physiol.* 1952; 117:77–86. PMID: [14946730](https://pubmed.ncbi.nlm.nih.gov/14946730/)
31. Leonard TR, Herzog W. Regulation of muscle force in the absence of actin-myosin-based cross-bridge interaction. *Am J Physiol Cell Physiol.* 2010; 299(1):C14–20. Epub 2010/04/02. doi: ajpcell.00049.2010 [pii] doi: [10.1152/ajpcell.00049.2010](https://doi.org/10.1152/ajpcell.00049.2010) PMID: [20357181](https://pubmed.ncbi.nlm.nih.gov/20357181/).
32. Herzog W, Leonard TR. Depression of cat soleus-forces following isokinetic shortening. *J Biomech.* 1997; 30(9):865–72. PMID: [9302608](https://pubmed.ncbi.nlm.nih.gov/9302608/)
33. Herzog W, Leonard TR, Joumaa V, Mehta A. Mysteries of muscle contraction. *J Appl Biomech.* 2008; 24(1):1–13. PMID: [18309178](https://pubmed.ncbi.nlm.nih.gov/18309178/).
34. Edman KA. Contractile performance of striated muscle. *Adv Exp Med Biol.* 2010; 682:7–40. Epub 2010/09/09. doi: [10.1007/978-1-4419-6366-6_2](https://doi.org/10.1007/978-1-4419-6366-6_2) PMID: [20824518](https://pubmed.ncbi.nlm.nih.gov/20824518/).

35. Campbell SG, Campbell KS. Mechanisms Of Residual Force Enhancement In Skeletal Muscle: Insights From Experiments And Mathematical Models. *Biophys Rev.* 2011; 3(4):199–207. Epub 2011/12/20. doi: [10.1007/s12551-011-0059-2](https://doi.org/10.1007/s12551-011-0059-2) PMID: [22180761](https://pubmed.ncbi.nlm.nih.gov/22180761/).
36. Morgan DL, Mochon S, Julian FJ. A quantitative model of intersarcomere dynamics during fixed-end contractions of single frog muscle fibers. *Biophys J.* 1982; 39(2):189–96. PMID: [6981436](https://pubmed.ncbi.nlm.nih.gov/6981436/)
37. Campbell SG, Hatfield PC, Campbell KS. A mathematical model of muscle containing heterogeneous half-sarcomeres exhibits residual force enhancement. *PLoS Comput Biol.* 2011; 7(9):e1002156. Epub 2011/10/08. doi: [10.1371/journal.pcbi.1002156](https://doi.org/10.1371/journal.pcbi.1002156) PCOMPBIOL-D-11-00502 [pii]. PMID: [21980268](https://pubmed.ncbi.nlm.nih.gov/21980268/).
38. Till O, Siebert T, Blickhan R. A mechanism accounting for independence on starting length of tension increase in ramp stretches of active skeletal muscle at short half-sarcomere lengths. *J Theor Biol.* 2010; 266(1):117–23. Epub 2010/07/06. doi: [S0022-5193\(10\)00311-5](https://doi.org/S0022-5193(10)00311-5) [pii] doi: [10.1016/j.jtbi.2010.06.021](https://doi.org/10.1016/j.jtbi.2010.06.021) PMID: [20600144](https://pubmed.ncbi.nlm.nih.gov/20600144/).
39. Bobbert MF, Huijting PA, van Ingen Schenau GJ. A model of the human triceps surae muscle-tendon complex applied to jumping. *J Biomech.* 1986; 19(11):887–98. Epub 1986/01/01. PMID: [3793737](https://pubmed.ncbi.nlm.nih.gov/3793737/).
40. Lieber RL, Blevins FT. Skeletal muscle architecture of the rabbit hindlimb: functional implications of muscle design. *J Morphol.* 1989; 199(1):93–101. Epub 1989/01/01. doi: [10.1002/jmor.1051990108](https://doi.org/10.1002/jmor.1051990108) PMID: [2921772](https://pubmed.ncbi.nlm.nih.gov/2921772/).
41. Prilutsky BI, Herzog W, Allinger TL. Mechanical power and work of cat soleus, gastrocnemius and plantaris muscles during locomotion: possible functional significance of muscle design and force patterns. *J Exp Biol.* 1996; 199(Pt 4):801–14. PMID: [8788087](https://pubmed.ncbi.nlm.nih.gov/8788087/).
42. Böhl M, Kruse R, Ehret AE, Leichsenring K, Siebert T. Compressive properties of passive skeletal muscle—The impact of precise sample geometry on parameter identification in inverse finite element analysis. *J Biomech.* 2012; 45(15):2673–9. Epub 2012/09/08. doi: [S0021-9290\(12\)00471-X](https://doi.org/S0021-9290(12)00471-X) [pii] doi: [10.1016/j.jbiomech.2012.08.023](https://doi.org/10.1016/j.jbiomech.2012.08.023) PMID: [22954714](https://pubmed.ncbi.nlm.nih.gov/22954714/).
43. Böhl M, Leichsenring K, Weichert C, Sturmat M, Schenk P, Blickhan R, et al. Three-dimensional surface geometries of the rabbit soleus muscle during contraction: input for biomechanical modelling and its validation. *Biomech Model Mechanobiol.* 2013; 12(6):1205–20. Epub 2013/02/19. doi: [10.1007/s10237-013-0476-1](https://doi.org/10.1007/s10237-013-0476-1) PMID: [23417261](https://pubmed.ncbi.nlm.nih.gov/23417261/).
44. van Zandwijk JP, Baan GC, Bobbert MF, Huijting PA. Evaluation of a self-consistent method for calculating muscle parameters from a set of isokinetic releases. *Biol Cybern.* 1997; 77(4):277–81. PMID: [9394445](https://pubmed.ncbi.nlm.nih.gov/9394445/).
45. Till O, Siebert T, Rode C, Blickhan R. Characterization of isovelocity extension of activated muscle: a Hill-type model for eccentric contractions and a method for parameter determination. *J Theor Biol.* 2008; 255(2):176–87. PMID: [18771670](https://pubmed.ncbi.nlm.nih.gov/18771670/). doi: [10.1016/j.jtbi.2008.08.009](https://doi.org/10.1016/j.jtbi.2008.08.009)
46. Wank V. Modellierung und Simulation von Muskelkontraktionen für die Diagnose von Kraftfähigkeiten. Köln: Sport und Buch Strauss; 1996.
47. Otten E. A myocybernetic model of the jaw system of the rat. *J Neurosci Methods.* 1987; 21(2–4):287–302. PMID: [3682879](https://pubmed.ncbi.nlm.nih.gov/3682879/).
48. Brown IE, Scott SH, Loeb GE. Mechanics of feline soleus: II. Design and validation of a mathematical model. *J Muscle Res Cell Motil.* 1996; 17(2):221–33. PMID: [8793724](https://pubmed.ncbi.nlm.nih.gov/8793724/)
49. Böck P. Romeis: Mikroskopische Technik 17. Auflage ed. München: Urban & Schwarzenberg; 1989.
50. Schilling N, Stark H, Fischer MS. Analyse der paravertebralen Muskulatur kleiner Säugetiere. In: Grieshaber R, Schneider W, editors. Prävention von arbeitsbedingten Gesundheitsgefahren und Erkrankungen. Leipzig: Monade Agentur für Kommunikation,; 2003. p. 343–54.
51. Cohen J. Statistical power analysis for the behavioral sciences. Hillsdale, NJ Lawrence Erlbaum Associates; 1988.
52. Mendez J, Keys A. Density and composition of mammalian muscle. *Metabolism.* 1960; 9:184–8.
53. Asmussen G, Marechal G. Maximal shortening velocities, isomyosins and fibre types in soleus muscle of mice, rats and guinea-pigs. *J Physiol.* 1989; 416:245–54. Epub 1989/09/01. PMID: [2607450](https://pubmed.ncbi.nlm.nih.gov/2607450/).
54. Stark H, Schilling N. A novel method of studying fascicle architecture in relaxed and contracted muscles. *J Biomech.* 2010; 43(15):2897–903. Epub 2010/08/31. doi: [S0021-9290\(10\)00422-7](https://doi.org/S0021-9290(10)00422-7) [pii] doi: [10.1016/j.jbiomech.2010.07.031](https://doi.org/10.1016/j.jbiomech.2010.07.031) PMID: [20800841](https://pubmed.ncbi.nlm.nih.gov/20800841/).
55. Biewener AA, Blickhan R, Perry AK, Heglund NC, Taylor CR. Muscle forces during locomotion in kangaroo rats: force platform and tendon buckle measurements compared. *J Exp Biol.* 1988; 137:191–205. PMID: [3209966](https://pubmed.ncbi.nlm.nih.gov/3209966/)
56. Barclay CJ. Mechanical efficiency and fatigue of fast and slow muscles of the mouse. *J Physiol.* 1996; 497(Pt 3):781–94. PMID: [9003563](https://pubmed.ncbi.nlm.nih.gov/9003563/)

57. Luff AR. Dynamic properties of the inferior rectus, extensor digitorum longus, diaphragm and soleus muscles of the mouse. *J Physiol*. 1981; 313:161–71. Epub 1981/01/01. PMID: [7277215](#).
58. Wang LC, Kernell D. Fibre type regionalisation in lower hindlimb muscles of rabbit, rat and mouse: a comparative study. *J Anat*. 2001; 199(Pt 6):631–43. Epub 2002/01/15. PMID: [11787817](#); PubMed Central PMCID: PMC1468381.
59. Winters TM, Takahashi M, Lieber RL, Ward SR. Whole muscle length-tension relationships are accurately modeled as scaled sarcomeres in rabbit hindlimb muscles. *J Biomech*. 2011; 44(1):109–15. Epub 2010/10/05. doi: [10.1016/j.jbiomech.2010.08.033](#) S0021-9290(10)00479-3 [pii]. PMID: [20889156](#); PubMed Central PMCID: PMC3003754.
60. Ettema GJ, Huijing PA. Effects of distribution of muscle fiber length on active length-force characteristics of rat gastrocnemius medialis. *Anat Rec*. 1994; 239(4):414–20. PMID: [7978365](#)
61. Martin BR, Burr DB, Sharkey NA. *Skeletal tissue mechanics*. New York: Springer; 1998.
62. Wang JH. *Mechanobiology of tendon*. *J Biomech*. 2006; 39(9):1563–82. PMID: [16000201](#).
63. Monti RJ, Roy RR, Zhong H, Edgerton VR. Mechanical properties of rat soleus aponeurosis and tendon during variable recruitment in situ. *J Exp Biol*. 2003; 206(Pt 19):3437–45. PMID: [12939374](#).
64. Scott SH, Brown IE, Loeb GE. Mechanics of feline soleus: I. Effect of fascicle length and velocity on force output. *J Muscle Res Cell Motil*. 1996; 17:207–19. PMID: [8793723](#)
65. Brown IE, Cheng EJ, Loeb GE. Measured and modeled properties of mammalian skeletal muscle. II. The effects of stimulus frequency on force-length and force-velocity relationships. *J Muscle Res Cell Motil*. 1999; 20(7):627–43. PMID: [10672511](#).
66. Prado LG, Makarenko I, Andresen C, Kruger M, Opitz CA, Linke WA. Isoform diversity of giant proteins in relation to passive and active contractile properties of rabbit skeletal muscles. *J Gen Physiol*. 2005; 126(5):461–80. PMID: [16230467](#).
67. Edman KA, Elzinga G, Noble MI. Enhancement of mechanical performance by stretch during tetanic contractions of vertebrate skeletal muscle fibres. *J Physiol*. 1978; 281:139–55. PMID: [309001](#)
68. Biewener AA, McGowan C, Card GM, Baudinette RV. Dynamics of leg muscle function in tammar wallabies (*M. eugenii*) during level versus incline hopping. *J Exp Biol*. 2004; 207(Pt 2):211–23. Epub 2003/12/12. PMID: [14668306](#).
69. Jacobs R, Bobbert MF, van Ingen Schenau GJ. Function of mono- and biarticular muscles in running. *Med Sci Sports Exerc*. 1993; 25(10):1163–73. PMID: [8231762](#)
70. Biewener AA. Muscle function in vivo: a comparison of muscles used for elastic energy storage savings versus muscles used to generate power. *Am Zool*. 1998; 38:703–17.
71. Sinha S, Sinha U, Edgerton VR. In vivo diffusion tensor imaging of the human calf muscle. *J Magn Reson Imaging*. 2006; 24(1):182–90. Epub 2006/05/27. doi: [10.1002/jmri.20593](#) PMID: [16729262](#).
72. Kermarrec E, Budzik JF, Khalil C, Le Thuc V, Hancart-Destee C, Cotten A. In vivo diffusion tensor imaging and tractography of human thigh muscles in healthy subjects. *AJR Am J Roentgenol*. 2010; 195(5):W352–6. Epub 2010/10/23. doi: [10.2214/AJR.09.3368](#) 195/5/W352 [pii]. PMID: [20966300](#).
73. Froeling M, Oudeman J, van den Berg S, Nicolay K, Maas M, Strijkers GJ, et al. Reproducibility of diffusion tensor imaging in human forearm muscles at 3.0 T in a clinical setting. *Magn Reson Med*. 2010; 64(4):1182–90. Epub 2010/08/21. doi: [10.1002/mrm.22477](#) PMID: [20725932](#).
74. Heemskerk AM, Strijkers GJ, Vilanova A, Drost MR, Nicolay K. Determination of mouse skeletal muscle architecture using three-dimensional diffusion tensor imaging. *Magn Reson Med*. 2005; 53(6):1333–40. PMID: [15906281](#).
75. Stark H, Frober R, Schilling N. Intramuscular architecture of the autochthonous back muscles in humans. *J Anat*. 2013; 222(2):214–22. Epub 2012/11/06. doi: [10.1111/joa.12005](#) PMID: [23121477](#); PubMed Central PMCID: PMC3632226.
76. Hiepe P, Herrmann KH, Gullmar D, Ros C, Siebert T, Blickhan R, et al. Fast low-angle shot diffusion tensor imaging with stimulated echo encoding in the muscle of rabbit shank. *NMR Biomed*. 2014; 27(2):146–57. Epub 2013/10/24. doi: [10.1002/nbm.3046](#) PMID: [24151092](#).
77. Binkhorst RA, t Hof MAV. Force-velocity relationship and contraction time of the rat fast plantaris muscle due to compensatory hypertrophy. *Pflugers Arch*. 1973; 342(2):145–58. Epub 1973/08/17. PMID: [4795635](#).
78. Savelberg HH, Willems PJ, Baan GC, Huijing PA. Deformation and three-dimensional displacement of fibers in isometrically contracting rat plantaris muscles. *J Morphol*. 2001; 250(1):89–99. Epub 2001/10/13. doi: [10.1002/jmor.1061](#) [pii] 10.1002/jmor.1061. PMID: [11599018](#).
79. Sacks RD, Roy RR. Architecture of the hind limb muscles of cats: functional significance. *J Morphol*. 1982; 173(2):185–95. PMID: [7120421](#).

80. Paxton H, Anthony NB, Corr SA, Hutchinson JR. The effects of selective breeding on the architectural properties of the pelvic limb in broiler chickens: a comparative study across modern and ancestral populations. *J Anat.* 2010; 217(2):153–66. Epub 2010/06/19. doi: [10.1111/j.1469-7580.2010.01251.x](https://doi.org/10.1111/j.1469-7580.2010.01251.x) JOA1251 [pii]. PMID: [20557402](https://pubmed.ncbi.nlm.nih.gov/20557402/); PubMed Central PMCID: PMC2913024.
81. Yucesoy CA, Koopman BH, Baan GC, Grootenboer HJ, Huijing PA. Extramuscular myofascial force transmission: experiments and finite element modeling. *Arch Physiol Biochem.* 2003; 111(4):377–88. Epub 2005/03/15. doi: NYMCO7BLYF62B0H [pii] doi: [10.3109/13813450312331337630](https://doi.org/10.3109/13813450312331337630) PMID: [15764078](https://pubmed.ncbi.nlm.nih.gov/15764078/).
82. Siebert T, Till O, Blickhan R. Work partitioning of transversally loaded muscle: experimentation and simulation. *Comput Methods Biomech Biomed Engin.* 2014; 17(3):217–29. Epub 2012/04/21. doi: [10.1080/10255842.2012.675056](https://doi.org/10.1080/10255842.2012.675056) PMID: [22515574](https://pubmed.ncbi.nlm.nih.gov/22515574/).
83. Siebert T, Till O, Stutzig N, Gunther M, Blickhan R. Muscle force depends on the amount of transversal muscle loading. *J Biomech.* 2014; 47:1822–8. Epub 2014/04/15. doi: S0021-9290(14)00199-7 [pii] doi: [10.1016/j.jbiomech.2014.03.029](https://doi.org/10.1016/j.jbiomech.2014.03.029) PMID: [24725439](https://pubmed.ncbi.nlm.nih.gov/24725439/).
84. Hides JA, Stokes MJ, Saide M, Jull GA, Cooper DH. Evidence of lumbar multifidus muscle wasting ipsilateral to symptoms in patients with acute/subacute low back pain. *Spine (Phila Pa 1976).* 1994; 19(2):165–72. Epub 1994/01/15. PMID: [8153825](https://pubmed.ncbi.nlm.nih.gov/8153825/).
85. Mengiardi B, Schmid MR, Boos N, Pfirrmann CW, Brunner F, Elfering A, et al. Fat content of lumbar paraspinal muscles in patients with chronic low back pain and in asymptomatic volunteers: quantification with MR spectroscopy. *Radiology.* 2006; 240(3):786–92. Epub 2006/08/24. doi: 240/3/786 [pii] doi: [10.1148/radiol.2403050820](https://doi.org/10.1148/radiol.2403050820) PMID: [16926328](https://pubmed.ncbi.nlm.nih.gov/16926328/).
86. Mannion AF, Weber BR, Dvorak J, Grob D, Muntener M. Fibre type characteristics of the lumbar paraspinal muscles in normal healthy subjects and in patients with low back pain. *J Orthop Res.* 1997; 15(6):881–7. Epub 1998/03/14. doi: [10.1002/jor.1100150614](https://doi.org/10.1002/jor.1100150614) PMID: [9497814](https://pubmed.ncbi.nlm.nih.gov/9497814/).